

High-Order Fractal Quantum Oscillations in Graphene/BN Superlattices in the Extreme Doping Limit

Wu Shi^{1,2,3,4,5,*} Salman Kahn^{3,4,5} Nicolas Leconte⁶ Takashi Taniguchi,⁷ Kenji Watanabe⁷
Michael Crommie^{3,4,5} Jeil Jung^{6,8} and Alex Zettl^{3,4,5,†}

¹State Key Laboratory of Surface Physics and Institute for Nanoelectronic Devices and Quantum Computing, Fudan University, Shanghai 200433, China

²Zhangjiang Fudan International Innovation Center, Fudan University, Shanghai 201210, China

³Department of Physics, University of California, Berkeley, California 94720, USA

⁴Materials Sciences Division, Lawrence Berkeley National Laboratory, Berkeley, California 94720, USA

⁵Kavli Energy NanoSciences Institute at the University of California and the Lawrence Berkeley National Laboratory, Berkeley, California 94720, USA

⁶Department of Physics, University of Seoul, Seoul 02504, Korea

⁷National Institute for Materials Science, 1-1 Namiki, Tsukuba 305-0044, Japan

⁸Department of Smart Cities, University of Seoul, Seoul 02504, Korea



(Received 12 January 2022; revised 23 January 2023; accepted 3 April 2023; published 3 May 2023)

Recent studies of van der Waals (vdW) heterostructures and superlattices have shown intriguing quantum phenomena, but these have been largely explored only in the moderate carrier density regime. Here, we report the probe of high-temperature fractal Brown-Zak (BZ) quantum oscillations through magnetotransport in the extreme doping regimes by applying a newly developed electron beam doping technique. This technique gives access to both ultrahigh electron and hole densities beyond the dielectric breakdown limit in graphene/BN superlattices, enabling the observation of nonmonotonic carrier-density dependence of fractal BZ states and up to fourth-order fractal BZ features despite strong electron-hole asymmetry. Theoretical tight-binding simulations qualitatively reproduce all observed fractal BZ features and attribute the nonmonotonic dependence to the weakening of superlattice effects at high carrier densities.

DOI: [10.1103/PhysRevLett.130.186204](https://doi.org/10.1103/PhysRevLett.130.186204)

van der Waals (vdW) heterostructures formed from disparate materials provide an exciting platform for unparalleled materials design and device innovation [1–3]. Recent advances in controlling the rotational orientation of vdW layers have led to moiré superlattices and associated interaction driven phenomena such as the fractional fractal quantum Hall effect, high-temperature quantum oscillations, correlated insulating states, magic-angle superconductivity, and quantum anomalous Hall effects [4–14]. A key control parameter is the carrier density, most commonly altered via field effect gating. However, conventional field effect gating (by applying a gate bias through the solid dielectric layer) has unavoidable limitations, such as those imposed by dielectric breakdown, which hinders further exploration of ultrahigh carrier density regimes. More effective doping techniques are called for in exploring new physics. For example, high-temperature quantum oscillations have been reported in graphene/h-BN superlattices [8,9]. These so-called Brown-Zak (BZ) oscillations originate from periodic emergence of delocalized Bloch states when the magnetic length is commensurate with the lattice periodicity, and can in principle occur for all rational fractions of magnetic flux $\phi = \phi_0 p/q$, where ϕ_0 is the flux quantum, and p and q are integer numbers [9,15,16].

In order to probe high-order fractal BZ states, high carrier densities and high magnetic fields are preferred. Kumar and collaborators achieved high electron densities by using a photodoping technique and revealed fractal BZ states up to fourth order with magnetic fields up to 30 T [9]. However, further observation of these high-order fractal states in the extreme doping limit has not been demonstrated due to the inefficiency of hole doping for the photodoping technique [17,18] and low visibility of BZ states originated from electron-hole asymmetry in graphene/h-BN superlattices [8].

Here we explore the extended carrier density parameter space in graphene/h-BN superlattices accessed by a recently developed electron-beam doping technique [19]. We uncover fractal BZ oscillations up to fourth order in the previously inaccessible highly electron and hole doped regimes with a moderate magnetic field of up to 9 T. A wide-range carrier density spectrum of the fractal BZ features is established, revealing unexpected nonmonotonic carrier-density dependence and strong electron-hole asymmetry of fractal BZ states. Our tight-binding calculations qualitatively reproduce all observed fractal BZ features and attribute the non-monotonic behavior to the weakening of superlattice effects at high carrier densities. Our results demonstrate the effectiveness of the electron-beam doping

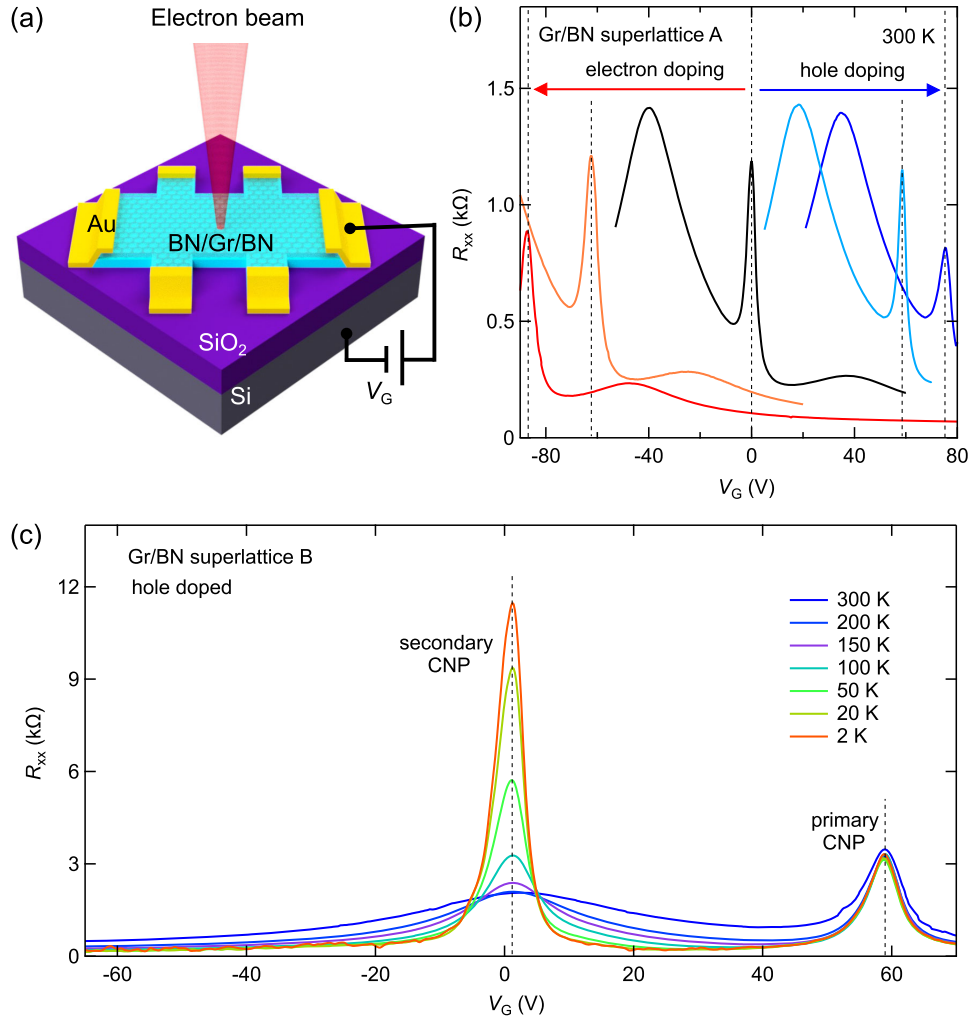


FIG. 1. (a) Experimental scheme for the electron-beam induced doping in graphene/h-BN superlattice device. Charge doping is induced in graphene by electron beam irradiation in a standard SEM for a few seconds while holding the back-gate $V_G = V_{\text{SET}} (\neq 0)$. (b) Transfer curves of a graphene/h-BN superlattice (device A) after e-beam doping by controlling the e -beam energy and the V_{SET} value. For the data indicated, the e -beam energy is 30 keV and $V_{\text{SET}} = 40, 30, -30$, and -40 V (from red to blue curves, skipping the black curve), respectively. The black curve is measured for the pristine device before any e -beam exposure. (c) Transfer curves of another graphene/h-BN superlattice (device B) after highly hole-doped measured from 300 to 2 K.

technique and provide new opportunities in exploring vdW heterostructures and superlattices in previously inaccessible high carrier density regimes.

The experimental scheme for electron-beam induced doping in the graphene/h-BN superlattice with edge contacts [20] is shown in Fig. 1(a). Charge doping is induced by electron beam irradiation in a standard scanning electron microscopy (SEM) for a few seconds while holding the back-gate $V_G = V_{\text{SET}} (\neq 0)$. By changing the sign and magnitude of V_{SET} during exposure, specific electron or hole doping can be controllably induced. The doped state persists even after the electron beam and backgate are removed. The process is reversible and repeatable so we can successively induce highly electron or hole doped states in a single device and systematically investigate the transport properties [19].

High carrier densities beyond $\pm 10^{13} \text{ cm}^{-2}$ can be reliably induced with this technique in graphene/h-BN superlattice devices. This exceeds the conventional electrostatic gating limit of $\sim \pm 5 \times 10^{12} \text{ cm}^{-2}$. Figure 1(b) shows the e -beam doping effects of a graphene/h-BN superlattice (device A) after 30 keV e -beam irradiation at $V_{\text{SET}} = 40, 30, -30$, and -40 V (from red to blue curves, skipping the black curve), respectively. The black curve is measured from the pristine device before the e -beam exposure. From the transfer curves, the primary charge neutrality point (CNP) positions (marked by the dashed lines) are shifted simultaneously with the secondary CNPs to positive and negative sides after irradiation, indicating effective hole and electron doping, respectively. The large CNP shift ΔV_{CNP} over 160 V clearly demonstrates strong tunability of carrier density across a range more than 10^{13} cm^{-2} by

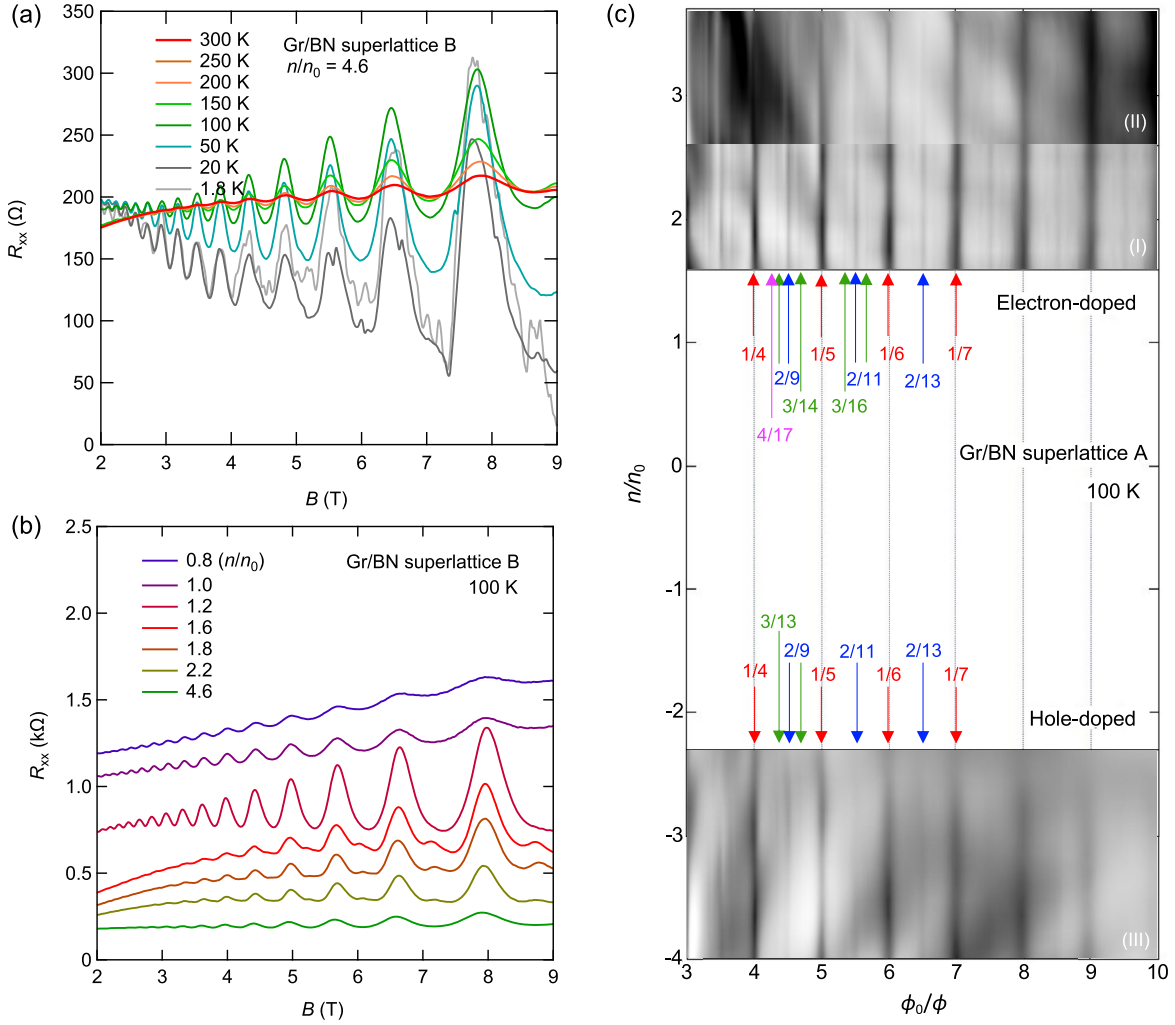


FIG. 2. Brown-Zak (BZ) oscillations in electron-doped and hole-doped graphene/h-BN superlattice device. (a) Longitudinal resistivity R_{xx} for device B as a function of magnetic field B at various temperatures from 300 to 1.8 K. The device is highly electron-doped by e-beam doping technique with a carrier density at $n = 4.6n_0$ ($\sim 1.7 \times 10^{13} \text{ cm}^{-2}$). (b) R_{xx} as a function of B at various electron densities measured at 100 K. (c) Longitudinal conductivity $\Delta\sigma_{xx}$ for device A as a function of ϕ_0/ϕ and n/n_0 for high electron and hole doping in B up to 9 T measured at 100 K. $\Delta\sigma_{xx}$ is obtained by subtracting a smooth background from σ_{xx} . Logarithmic gray scale: white: -1.0 mS ; black: 1.5 mS . The red, blue, green, and pink arrows indicate the primary and fractal states with $p = 1, 2, 3$, and 4 , respectively.

the electron-beam doping technique, which typically cannot be achieved with a conventional SiO_2 backgated device. Remarkably, the graphene device still maintains high mobility after doping even though the CNP peak slightly broadens as the doping increases [19]. Figure 1(c) shows the temperature dependent transfer curves of another graphene/h-BN superlattice (device B) after hole doping induced by 30 keV e -beam irradiation at $V_{\text{SET}} = -30 \text{ V}$. The primary CNP shifts to $\sim 60 \text{ V}$ and remains unchanged while the secondary CNP in the hole side becomes more pronounced as temperature decreases, in agreement with an earlier report [4]. It demonstrates that the 30 keV e -beam induced doping is robust against temperature variations and preserves the moiré superlattice. From the primary and secondary CNP positions, we derive the full-filling carrier density for the superlattice $n_0 = 2.3 \times 10^{12}$ and

$3.8 \times 10^{12} \text{ cm}^{-2}$ for devices A and B, respectively (Fig. S1 [21]). From the relation $n_0 = 4/S = 8/(\sqrt{3}a^2)$ [8,9], the superlattice a is estimated to be 14 nm (device A) and 10.9 nm (device B). Here, S is the area of the superlattice unit cell.

We present magnetotransport data for a highly electron-doped graphene/h-BN superlattice induced by the electron-beam doping technique. Figure 2(a) shows the longitudinal resistivity R_{xx} for device B at a high electron density of $n = 4.6n_0 = 1.7 \times 10^{13} \text{ cm}^{-2}$ as a function of magnetic field B at various temperatures. A strong periodic oscillation of the magnetoresistance is clearly seen even at 300 K with a magnetic field up to 9 T and it becomes further enhanced as temperature decreases. These high temperature magneto-oscillations are a manifestation of BZ oscillations, which have been described previously but characterized

only in a much lower carrier density regime [8,9]. At temperatures below 20 K, Shubnikov–de Haas (SdH) oscillations arise and overlay with the BZ oscillations evidenced by the appearance of additional oscillation peaks as shown in Fig. 2(a). One essential feature of BZ oscillations that differs from SdH oscillations is that the BZ oscillation periodicity is independent of the carrier density. This can be seen from Fig. 2(b), which shows R_{xx} as a function of B for device B at various electron densities from $n = 0.8n_0$ to $4.6n_0$. We see clearly that the oscillation periodicity remains unchanged across a wide carrier density range up to $1.7 \times 10^{13} \text{ cm}^{-2}$. The oscillation amplitude increases as n increases beyond the secondary CNP ($n = n_0$) [8,9] and becomes most pronounced near the third-generation CNP ($n = 2n_0$). Additionally, we observe second-order fractal oscillations as the electron density nears the third-generation CNP but the fractal periodicity becomes less visible at higher density at $n = 4.6n_0$.

To clearly see the fractal oscillations, we carefully tune the carrier density of the graphene/h-BN superlattice across extreme electron and hole doping limits using the electron-beam doping technique. We measure the magneto-transport of device A at various carrier densities between $3.7n_0$ to $-4.0n_0$ (negative for hole-doping), and plot a map of longitudinal conductivity $\Delta\sigma_{xx}$ as a function of n and $1/B$ (in units of ϕ_0/ϕ) with a maximum B field up to 9 T as shown in Fig. 2(c). Here $\Delta\sigma_{xx}$ is obtained by subtracting a smooth background from the longitudinal conductivity σ_{xx} . The magnetic flux through the superlattice unit cell is $\phi = BS$. The data are taken from three sets of experiments after electron-beam doping on the same device, which results in varied backgrounds but the oscillation features match up with each other. We observe a set of dark vertical streaks (marked by the red arrows) indicating local maxima of conductivity located at $\phi/\phi_0 = 1/q$ (q is an integer) in both highly electron-doped and hole-doped regimes, which corresponds to a magnetic flux quantum ϕ_0 per q superlattice unit cells. The oscillations are periodic in $1/\phi$ (i.e., $1/B$) with an oscillation frequency $B_0 = \phi_0/S = n_0\phi_0/4 \sim 24 \text{ T}$, which is consistent with the value calculated from the Fourier transform of the magneto-conductivity data. Additional local maxima at $\phi/\phi_0 = p/q$, where p magnetic flux quantum ϕ_0 pierces through q superlattice unit cells mimicking zero effective magnetic field for the transport [8], are also observed as thinner vertical streaks (marked by the blue, green and pink arrows) between the thick streaks at higher magnetic field regime, independent of the carrier density. These extra fractal features located at $\phi/\phi_0 = p/q$ are caused by high-order magnetic Bloch states with $p = 2, 3$, and 4.

To better resolve these high-order fractal oscillations, we plot the original longitudinal magnetoconductivity σ_{xx} (without background subtraction) as a function of ϕ_0/ϕ for device A at various electron densities in Fig. 3(a). The data are taken at 100 K and a magnetic field up to 9 T.

The electron density, n , increases from $1.6n_0$ to $2.6n_0$ with a step of $\sim 0.14n_0$ [from the bottom to top in Fig. 3(a)]. We see that extra conductivity maxima gradually emerge as n increases and become prominent near the third-generation CNP with $n \sim 2n_0$. We have identified these states (marked by vertical dash lines and arrows) with exact p and q values up to the fourth order ($p = 4$). At 100 K, as n further increases up to $3.7n_0$, these higher-order fractions are less visible or are mixed with additional peaks and thus difficult to resolve (see Supplemental Material, Fig. S2 [21]). This is consistent with previous observation in device B [Fig. 2(b)]. Note that higher-order magnetic Bloch states with $p > 2$ are not seen in device B possibly because its moiré lattice is short (corresponding to larger B_0) and the magnetic field is not sufficiently high in our measurements (maximum field up to 9 T). Kumar's report that revealed the third- and fourth-order magnetic Bloch states used a high magnetic field up to 30 T [9].

Next, we focus on the high-order fractal BZ states in the highly hole-doped regime. At low hole density below the third-generation CNP with $n \sim -2n_0$, we observe only the primary maxima located with $p = 1$ (see Supplemental Material, Fig. S2 [21]). As the hole density further increases, extra local maximas with $p = 2, 3$, and 4 gradually appear, corresponding to second-, third-, and fourth-order fractal BZ oscillations as shown in Fig. 2(c). Here, the third- and fourth-order BZ oscillations with $p = 3$ and 4 are seen for the first time (marked by green and pink arrows), which is remarkable considering the much lower visibility of BZ oscillations for hole doping due to electron-hole asymmetry of electron-phonon scattering in graphene/BN superlattices [8]. Notably, these high-order fractal features are only visible at sufficiently high hole densities around -10^{13} cm^{-2} induced by the electron-beam doping technique, which is not accessible by conventional backgate tuning nor the photodoping technique.

In addition, these high-order fractal states are more pronounced when temperature decreases, as shown in Fig. 3(b) and 3(d). At $T = 200 \text{ K}$, only the $p = 1$ oscillations are visible while the higher order states with $p = 2, 3$, and 4 are more prominent at $T = 50 \text{ K}$. These high-order fractal BZ features also show nonmonotonic carrier density dependence. In Fig. 3(e), we plot the conductivity peak amplitude $\Delta\sigma_{xx}$ versus carrier density for certain fractal BZ states with $p = 2$ and 3 by subtracting a smooth background from σ_{xx} in Figs. 3(a) and 3(c). These peak amplitudes firstly increase as the carrier density increases and then gradually decreases or saturates above certain densities (at around $-3n_0$ for holes and around $2n_0$ for electrons). The peaks corresponding to fractal BZ features for holes appear at higher densities and have less maximum amplitude, also indicating the lower visibility of BZ states for hole doping.

To provide rationale to the experimental observations of nonmonotonic carrier density dependence, i.e., the

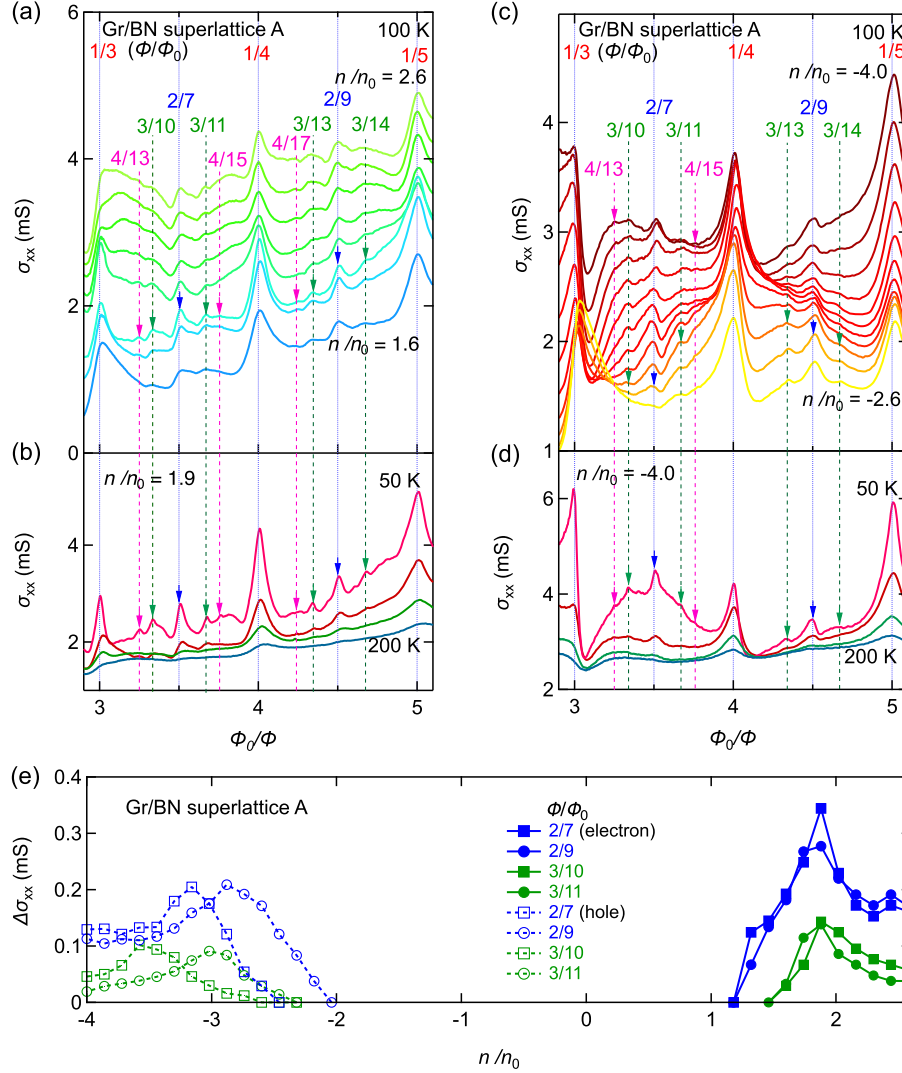


FIG. 3. High-order fractal BZ oscillations in highly electron-doped and hole-doped graphene/h-BN superlattice (device A). (a) Longitudinal conductivity σ_{xx} as a function of ϕ_0/ϕ measured at various electron densities n from $1.6n_0$ to $2.6n_0$ with a step of $\sim 0.14n_0$. (b) σ_{xx} as a function of ϕ_0/ϕ for $n = 1.9n_0$ at various temperatures from 200 to 50 K. (c) σ_{xx} as a function of ϕ_0/ϕ measured at various hole densities n from $-2.6n_0$ to $-4.0n_0$ with a step of $\sim 0.14n_0$. (d) σ_{xx} as a function of ϕ_0/ϕ for $n = -4.0n_0$ at various temperatures from 200 to 50 K. The vertical dashed lines and arrows indicate the magnetic field positions where the fractal BZ states with $p = 2, 3$, and 4 . (e) Conductivity peak amplitude $\Delta\sigma_{xx}$ versus carrier density for fractal BZ states with $p = 2$ and 3 . $\Delta\sigma_{xx}$ is obtained by subtracting a smooth background from σ_{xx} in (a) and (c).

relatively stronger fractal BZ oscillations for intermediate charge carrier densities and weakened features for high densities, we simulate a similarly aligned system using a tight-binding (TB) implementation of the Kubo formula for the longitudinal conductivity through wave-packet evolution [22–24]. This method allows us to straightforwardly probe qualitatively different transport behavior in the ballistic regime by following the mean quadratic displacement of the wave packets [25].

Our simulation reproduces nearly all primary and fractal BZ features that occur in the experiment. Figures 4(a) and 4(b) show the calculated conductivity as a function of ϕ_0/ϕ and n/n_0 for hole-doped and electron-doped graphene/h-BN superlattice with a lattice periodicity of 13.5 nm.

As indicated by the vertical lines, high-order fractal states with $p = 2, 3$, and 4 are clearly resolved for high hole and electron doping. In agreement with our experimental observations, the fractal BZ oscillations are less likely to be resolved at lowest charge carrier densities, due to the weaker density of states and reduced group velocity. This observation is slightly obfuscated by the robust Landau levels in our zero-temperature simulations. As the carrier density increases, we further observe an increase in the strength of the fractal BZ features, whereas it gradually becomes smeared at the highest charge carrier densities (also supported by Supplemental Material, Fig. S3 [21]), consistent with our experimental observation. This is because the larger the density of states (DOS), the fewer the superlattice

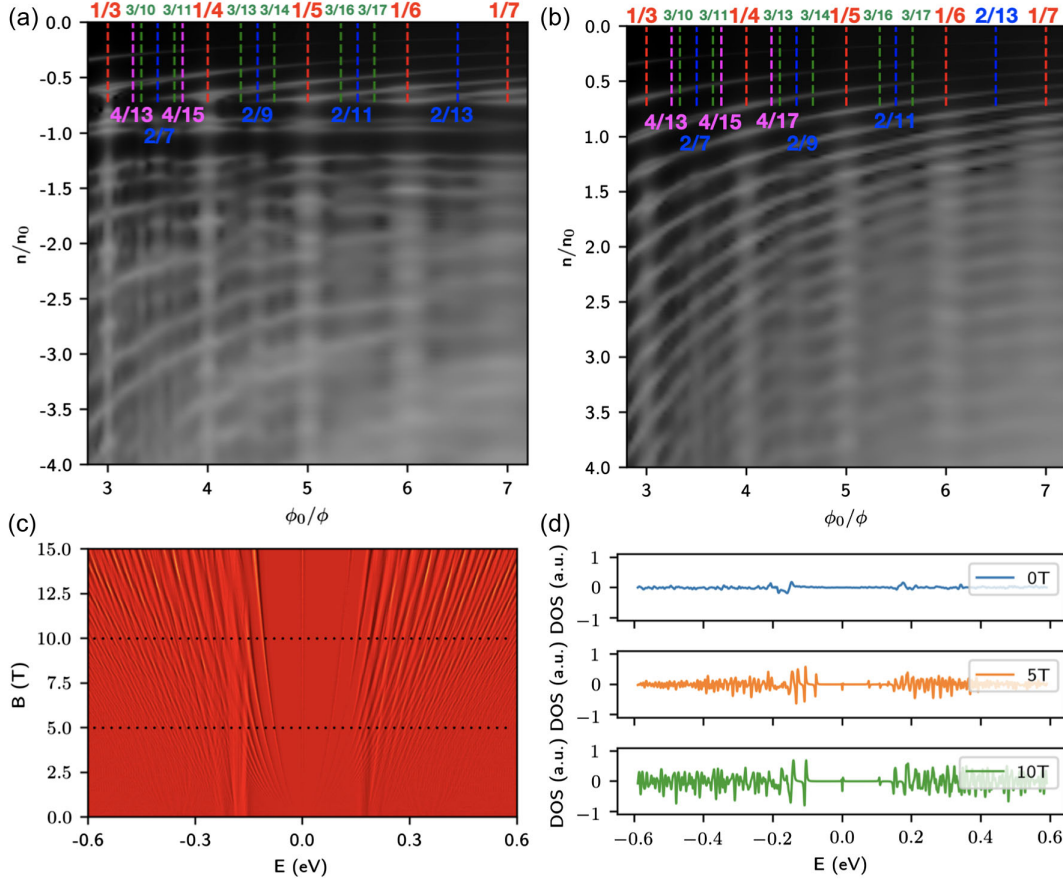


FIG. 4. Qualitative simulation of magnetoconductivity by a tight-binding method. The simulated conductivity of (a) hole-doped and (b) electron-doped graphene/h-BN superlattice plotted as a function of ϕ_0/ϕ and charge carrier density n/n_0 (negative for hole doping) clearly resolves the fractal BZ oscillations with $p = 2, 3$, and 4 , as indicated by the dashed vertical lines with the labels of corresponding q values. Landau level features are still seen in the background as the simulations occur at zero temperature. (c) The calculated density of states (DOS) with respect to the energy and the magnetic field for the graphene/h-BN superlattice after subtracting the DOS Landau level map of the pristine graphene system. (d) The DOS versus energy at different magnetic fields, obtained from the line cuts in (c). The secondary Dirac points with $n/n_0 = 1$ appear at the energy around ± 0.16 eV.

minibands carrying the fractal BZ oscillations with specific values of p and q that are separated in energy. The BZ oscillations occur at frequencies where the cyclotron orbit length scale becomes commensurate with the periodicity of the system. The existence of the former length scale gradually disappears at larger charge carrier density (cf. the gradually weaker Landau level quantization signatures), thus requiring larger magnetic fields to resolve them.

To verify this, we calculate the DOS with respect to the energy E (in proportion to \sqrt{n} , n is the carrier density) and the magnetic field B for pristine graphene as well as the graphene/h-BN superlattice system. We subtract the former from the latter to remove the Landau level features coming from the primary Dirac cone to keep only the superlattice features as shown in Fig. 4(c). This subtraction is not perfect due to the superlattice induced broadening of the Landau levels, but it is sufficient to capture how the superlattice effects evolve with the energies (or carrier density) and magnetic fields. Figure 4(d) shows a series of

line cuts at 0, 5, and 10 T from Fig. 4(c). As most of visible fractal BZ states appear in the magnetic field range of 4–8 T (Fig. 3), the line cut at 5 T represents the energy (or carrier density) dependence of superlattice effects in our experiments. It illustrates that the superlattice effects are weak close to the primary Dirac point energy (± 0.16 eV), become maximal around the secondary Dirac point energy and weaken again at higher energy (or carrier density) due to the increasing number of states with energy. This provides rationale for the weakened fractal BZ oscillations at high energies as the presence of fractal BZ is sensitive to the superlattice effects. The simulations also suggest that for higher magnetic field range, this weakening might only happen at even higher carrier density regime, which might be the reason it has not been probed by previous experiments [9]. In this study with a moderate magnetic field and high enough carrier density induced by electron-beam doping technique, we demonstrate that such a nonmonotonic behavior can be observed [21].

This work was supported primarily by the Director, Office of Science, Office of Basic Energy Sciences, Materials Sciences and Engineering Division, of the US Department of Energy under Contract No. DE-AC02-05-CH11231, within the van der Waals Heterostructures Program (KCWF16), which provided for design of the project, device fabrication, electron doping, and transport experiments. Additional support was provided by the Director, Office of Science, Office of Basic Energy Sciences, Materials Sciences and Engineering Division, of the US Department of Energy under Contract No. DE-AC02-05-CH11231, within the Nanomachines Program (KC1203), which provided for supplementary electron microscopy. W. S. was supported by the National Natural Science Foundation of China (Grant No. 12274090), the Natural Science Foundation of Shanghai (Grant No. 22ZR1406300) and a start-up grant from Fudan University. N. L. was supported by the Korean National Research Foundation Grant NRF-2020R1A2C3009142 and J. J. was supported by Grant No. NRF-2020R1A5A1016518. We acknowledge computational support from KISTI through Grant No. KSC-2022-CRE-0514, the resources of Urban Big data and AI Institute (UBAI) at the University of Seoul, and the network support through KREONET.

*Corresponding author.
shiwu@fudan.edu.cn

†Corresponding author.
azettl@berkeley.edu

- [1] A. K. Geim and I. V. Grigorieva, *Nature (London)* **499**, 419 (2013).
- [2] K. S. Novoselov, A. Mishchenko, A. Carvalho, and A. H. Castro Neto, *Science* **353**, 461 (2016).
- [3] Y. Liu, N. O. Weiss, X. Duan, H. C. Cheng, Y. Huang, and X. Duan, *Nat. Rev. Mater.* **1**, 16042 (2016).
- [4] L. A. Ponomarenko, R. V. Gorbachev, G. L. Yu, D. C. Elias, R. Jalil, A. A. Patel, A. Mishchenko, A. S. Mayorov, C. R. Woods, J. R. Wallbank, M. Mucha-Kruczynski, B. A. Piot, M. Potemski, I. V. Grigorieva, K. S. Novoselov, F. Guinea, V. I. Fal'ko, and A. K. Geim, *Nature (London)* **497**, 594 (2013).
- [5] B. Hunt, T. Taniguchi, P. Moon, M. Koshino, and R. C. Ashoori, *Science* **340**, 1427 (2013).
- [6] G. Chen, A. L. Sharpe, E. J. Fox, Y. H. Zhang, S. Wang, L. Jiang, B. Lyu, H. Li, K. Watanabe, T. Taniguchi, Z. Shi, T. Senthil, D. Goldhaber-Gordon, Y. Zhang, and F. Wang, *Nature (London)* **579**, 56 (2020).
- [7] C. R. Dean, L. Wang, P. Maher, C. Forsythe, F. Ghahari, Y. Gao, J. Katoch, M. Ishigami, P. Moon, M. Koshino, T. Taniguchi, K. Watanabe, K. L. Shepard, J. Hone, and P. Kim, *Nature (London)* **497**, 598 (2013).
- [8] R. K. Kumar, X. Chen, G. H. Auton, A. Mishchenko, D. A. Bandurin, S. V. Morozov, Y. Cao, E. Khestanova, M. Ben Shalom, A. V. Kretinin, K. S. Novoselov, L. Eaves, I. V. Grigorieva, L. A. Ponomarenko, V. I. Fal'ko, and A. K. Geim, *Science* **357**, 181 (2017).
- [9] R. K. Kumar, A. Mishchenko, X. Chen, S. Pezzini, G. H. Auton, L. A. Ponomarenko, U. Zeitler, L. Eaves, V. I. Fal'ko, and A. K. Geim, *Proc. Natl. Acad. Sci. U.S.A.* **115**, 5135 (2018).
- [10] Y. Cao, V. Fatemi, A. Demir, S. Fang, S. L. Tomarken, J. Y. Luo, J. D. Sanchez-Yamagishi, K. Watanabe, T. Taniguchi, E. Kaxiras, R. C. Ashoori, and P. Jarillo-Herrero, *Nature (London)* **556**, 80 (2018).
- [11] Y. Cao, V. Fatemi, S. Fang, K. Watanabe, T. Taniguchi, E. Kaxiras, and P. Jarillo-Herrero, *Nature (London)* **556**, 43 (2018).
- [12] E. Codecido, Q. Wang, R. Koester, S. Che, H. Tian, R. Lv, S. Tran, K. Watanabe, T. Taniguchi, F. Zhang, M. Bockrath, and C. N. Lau, *Sci. Adv.* **5**, 1 (2019).
- [13] L. Balents, C. R. Dean, D. K. Efetov, and A. F. Young, *Nat. Phys.* **16**, 725 (2020).
- [14] A. L. Sharpe, E. J. Fox, A. W. Barnard, J. Finney, K. Watanabe, T. Taniguchi, M. A. Kastner, and D. Goldhaber-Gordon, *Science* **365**, 605 (2019).
- [15] E. Brown, *Phys. Rev.* **133**, A1038 (1964).
- [16] J. Zak, *Phys. Rev.* **134**, A1602 (1964).
- [17] L. Ju, J. Velasco, E. Huang, S. Kahn, C. Nosiola, H. Z. Tsai, W. Yang, T. Taniguchi, K. Watanabe, Y. Zhang, G. Zhang, M. Crommie, A. Zettl, and F. Wang, *Nat. Nanotechnol.* **9**, 348 (2014).
- [18] J. Velasco, L. Ju, D. Wong, S. Kahn, J. Lee, H. Z. Tsai, C. Germany, S. Wickenburg, J. Lu, T. Taniguchi, K. Watanabe, A. Zettl, F. Wang, and M. F. Crommie, *Nano Lett.* **16**, 1620 (2016).
- [19] W. Shi, S. Kahn, L. Jiang, S. Y. Wang, H. Z. Tsai, D. Wong, T. Taniguchi, K. Watanabe, F. Wang, M. F. Crommie, and A. Zettl, *Nat. Electron.* **3**, 99 (2020).
- [20] L. Wang, I. Meric, P. Y. Huang, Q. Gao, Y. Gao, H. Tran, T. Taniguchi, K. Watanabe, L. M. Campos, D. A. Muller, J. Guo, P. Kim, J. Hone, K. L. Shepard, and C. R. Dean, *Science* **342**, 614 (2013).
- [21] See Supplemental Material at <http://link.aps.org/supplemental/10.1103/PhysRevLett.130.186204> for details on device fabrication, electron beam doping, magnetotransport measurements, and theoretical simulations, including Figs. S1–S3.
- [22] N. Leconte, A. Ferreira, and J. Jung, *Efficient Multiscale Lattice Simulations of Strained and Disordered Graphene*, 1st ed. (Elsevier Inc., New York, 2016).
- [23] Z. Fan, J. H. Garcia, A. W. Cummings, J. E. Barrios-Vargas, M. Panhans, A. Harju, F. Ortmann, and S. Roche, *Phys. Rep.* **903**, 1 (2021).
- [24] N. Leconte, A. Lherbier, F. Varchon, P. Ordejon, S. Roche, and J. C. Charlier, *Phys. Rev. B* **84**, 235420 (2011).
- [25] J. Jung, E. Laksono, A. M. Dasilva, A. H. Macdonald, M. Mucha-Kruczynski, and S. Adam, *Phys. Rev. B* **96**, 085442 (2017).